Sloshing of an ideal fluid in a horizontally forced rectangular tank

Lawrence K. Forbes

Abstract   The motion of an ideal fluid in a rectangular tank is studied, under conditions in which the tank is subjected to horizontal sinusoidal periodic forcing. A novel technique is presented for solving the problem; it makes use of a Fourier-series representation in which the time-dependent coefficients are shown to obey a system of forced nonlinear ordinary differential equations. Time-periodic solutions are computed using further Fourier-series representations and Newton's method to find the doubly subscripted arrays of coefficients. It is shown that the linearized solution describes the motion reasonably well, except near the regions of linearized resonance. A weakly nonlinear theory near resonance is presented, but is found to give a poor description of the motion. Extensive nonlinear results are shown which reveal intricate behaviour near resonance. A method is given for computing the stability of time-periodic solutions; it reveals that the solution branch corresponding to linearized theory is stable, but that additional unstable periodic solution branches may also be present. Further quasi-periodic and chaotic solutions are detected.

1 Introduction

The sloshing of fluid in a tank is a well-studied problem that has applications in a number of practical situations. As indicated by Virella et al. [1], the problem is relevant to the safety of transporting fluids in tankers; Hermann and Timokha [2] also stress its relevance to the automotive, aerospace and shipbuilding industries. Fluid sloshing in road tankers may result in overturning of the vehicle, and resonant movement of fluid within ship cargo tanks is also of concern. These practical considerations are discussed further in the review article by Ibrahim et al. [3]. They are reinforced by Frandsen [4], who also discusses the use of fluid-filled tanks to act as dampers on the motion of city buildings in high winds.

Chester [5] presented a mathematical analysis of the motion of the free surface in a tank of fluid subjected to horizontal periodic forcing. He identified points of resonance at which the forcing frequency is such that an odd number of half wavelengths fit along the tank. Linearized theory breaks down at resonance, since it assumes that the

L. K. Forbes (✉)
School of Mathematics and Physics, University of Tasmania, Private Bag 37, Hobart, TAS 7004, Australia
e-mail: Larry.Forbes@utas.edu.au

free-surface disturbances remain small, and Chester carried out a weakly nonlinear analysis near resonance. This was found by Chester and Bones [6] to be in at least qualitative agreement with experiment. They also suggested that nonlinearity could lead to unstable periodic solutions, and this has formed some of the motivation for the present work. Chester and Bones [6] found experimentally that there were parameter regions at which the motion of the interface became so irregular, where they expected to see sub-harmonic oscillations, that they abandoned further attempts to record its behaviour.

Ockendon and Ockendon [7] undertook an asymptotic analysis of the horizontal sloshing motion studied by Chester [5], and obtained a fourth-order nonlinear forced ordinary differential equation describing the motion near resonance. Their results indicated that the vertical resonant peaks of linearized theory were bent to one side by the effects of nonlinearity in a frequency-response diagram, so that multiple solutions might be expected near the resonance value. This is similar to the famous "hardening spring" or "softening spring" responses in the Duffing equation, as discussed, for example, by Seydel [8, p. 52].

Many authors have since applied weakly nonlinear asymptotic theories to study the behaviour of sloshing motion near resonance. Hill [9] and Hill and Frandsen [10] retained terms to third order in the wave amplitude and derived a cubic equation for amplitude in the vicinity of resonance. Three real solutions are possible on one side of the resonance peak and only one real solution on the other; thus the weakly nonlinear peak bends in the response curve, giving multiple solutions similar to those found by Ockendon and Ockendon [7]. Hysteresis behaviour is then possible near resonance, and has been found experimentally for horizontally excited shallow tanks by Gardarsson and Yeh [11]. Careful local analyses near the first two resonance regions have been carried out by Hermann and Timokha [2,12]. This work shows additional bifurcation behaviour in the vicinity of resonance. Amundsen et al. [13] used a forced Korteweg-de Vries approximation to model horizontally forced oscillations in a tank, and showed subtle and complex behaviour near resonance.

Fully numerical solutions have also been computed for tanks subject to horizontal forcing, vertical forcing (Faraday resonance), or a combination of both. Bredmose et al. [14] used a Boussinesq formulation of the governing equations and a finite-difference (method of lines) type scheme with filtering to model the problem mathematically. They also conducted extensive experiments, for both vertical and horizontal forcing, and showed reasonable agreement between the theoretical and measured results. For horizontally forced tanks, they observed 'violent' unsteady waves of very large amplitude. Frandsen [4] also used a finite-difference scheme to solve for free-surface motion in horizontally or vertically forced tanks, making use of a time-dependent transformation to map the fluid region onto a rectangle so that difference approximations could be applied. She computed periodic solutions as well as highly irregular ones, reminiscent of those evidently encountered experimentally by Chester and Bones [6]. A somewhat similar approach has also been adopted by Chen and Nokes [15], who used a finite-difference technique to solve the (viscous) incompressible Navier–Stokes equations after applying a simple transformation to map the fluid region onto the unit square. They likewise found irregular behaviour of the free surface, under periodic surge (horizontal) forcing. Viscosity was found to dampen the motion, but evidently did not alter the qualitative behaviour. A finite-element solution by Wang and Khoo [16] in the purely inviscid case also gives a similar outcome.

Numerical solutions with a more practical or engineering focus have been obtained with a variety of methods. The effects of viscosity and vertical baffles in the tank have been investigated by Celebi and Akyildiz [17] with a view to reducing the impact of 'violent' motion. Armenio and La Rocca [18] used a turbulence code to solve the Reynolds-averaged viscous equations for flow in a rectangular container, and obtained reasonable agreement with their experiments. Vertical baffles were again found to reduce wave motion significantly in the tank. Cariou and Casella [19] undertook a comparative study of a number of different numerical codes for solving sloshing problems, with the aim of addressing practical questions arising in industrial situations related to the operation of ships and tankers. They found that the codes were generally reliable for two-dimensional flows, and that fluid viscosity was not a major factor. Three-dimensional flows were still in need of further work, particularly as a result of the high demands they make on computer resources. Nevertheless, Liu and Lin [20] have recently obtained solutions for turbulent flow in three-dimensional geometry, and show computed solutions at different times for violent sloshing events. These solutions required 265 h of processor time on a high-performance computer.

Spectral ("modal") methods have also been used to solve the nonlinear equations for horizontal tank motion. Faltinsen et al. [21] and Faltinsen and Timokha [22] used a variational formulation of the inviscid irrotational flow equations with a spectral representation of the solution to Laplace's equation and computed nonlinear amplitude-response curves similar to those obtained by the weakly nonlinear theories. In a very thorough theoretical and experimental study, Ikeda [23] used a spectral technique to solve for the interaction of two liquid-filled tanks in an elastic structure. He obtained complex response curves in the case of vertical forcing, along with period-doubled and chaotic oscillations.

In the present paper, a spectral method is likewise used to solve the fully nonlinear equations of motion for the case of a horizontally excited tank. The technique has much in common with that used by Faltinsen et al. [21] but makes use of some extra novel features introduced by Forbes, Chen and Trenham [24] and used subsequently by Forbes and Hocking [25] to study fluid draining from a tank. Details of this solution procedure are outlined in Sect. 3. This technique allows time-periodic solutions to be computed directly; an approach based on the use of Floquet theory is presented in Sect. 4 for determining directly the stability of these periodic solutions. This formulation has the advantage that it permits even highly unstable solutions to be found accurately. It is also amenable to the derivation of weakly nonlinear solutions near resonance, and this is illustrated in the present problem in Sect. 5. Results are given in Sect. 6 for stable and unstable periodic nonlinear solutions and also for solutions that display quasi-periodic or chaotic irregular behaviour of the type remarked on by Chester and Bones [6]. Some concluding observations are given in Sect. 7.

2 The ideal-fluid model

Consider two-dimensional irrotational flow of an incompressible inviscid fluid. A velocity potential ϕ exists for the flow; its gradient gives the velocity vector in the form $(u, v) = (\partial\phi/\partial x, \partial\phi/\partial y)$. The functions u and v represent the components of the fluid velocity in the horizontal and vertical directions, respectively. Since the fluid is ideal, its velocity potential therefore satisfies Laplace's equation $\nabla^2\phi = 0$ at each point.

The fluid is situated in a rectangular tank. At rest, the origin of a coordinate system is located on the left wall of the tank at a height H above the bottom. The undisturbed fluid surface lies along the horizontal x-axis, the bottom is located on the plane $y = -H$ and the right wall of the tank is at position $x = L$. The fluid is affected by the downward acceleration g of gravity acting in the negative y-direction. The situation of interest here, however, is that in which the tank is subjected to sinusoidal horizontal forcing, with some amplitude A and frequency Ω.

It is appropriate to non-dimensionalize the problem at this point, and this is accomplished in this paper by referring all times to the quantity $1/\Omega$, choosing g/Ω as the unit of speed and thus g/Ω^2 as the scale for all lengths. This particular choice of dimensionless variables has been made so as to allow the freedom for the tank length and depth to be specified arbitrarily in the new variables, and even to approach infinity. These variables will be used from now on. In this formulation, there are three dimensionless parameter groups, defined as

$$\epsilon = \frac{\Omega^2 A}{g}; \quad \lambda = \frac{\Omega^2 L}{g}; \quad \beta = \frac{\Omega^2 H}{g}. \tag{2.1}$$

The first parameter ϵ represents the forcing amplitude of the horizontal motion. The remaining two parameters λ and β are, respectively, the tank length and depth.

The velocity potential ϕ satisfies Laplace's equation within the fluid, and is also subject to kinematic conditions on each bounding surface. As the fluid is inviscid, it is assumed to slip without hindrance on each boundary, so that

$$v = 0 \quad \text{on } y = -\beta \tag{2.2}$$

on the tank bottom. On the left and right tank walls, respectively, it is also the case that

$$\begin{aligned} u &= \epsilon \cos t \quad \text{on } x = \epsilon \sin t \\ u &= \epsilon \cos t \quad \text{on } x = \lambda + \epsilon \sin t. \end{aligned} \tag{2.3}$$
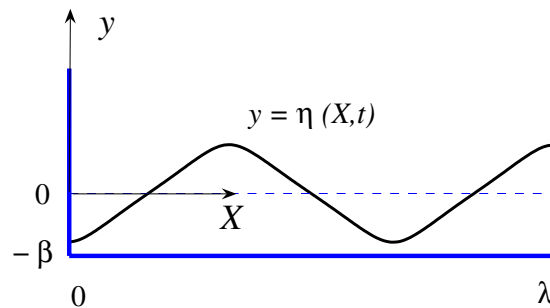
Fig. 1 A sketch of the dimensionless flow configuration in the non-inertial coordinates (X, y). The interface is taken from an actual solution with depth $\beta = 1$, forcing amplitude $\epsilon = 0.03$, response amplitude $A_T = 0.73$ (tank length $\lambda = 7.751735$). The scale on both axes is the same, so that this (unstable) periodic solution is as it would appear

The free surface of the fluid is represented by the equation $y = \eta(x, t)$, and is also subject to the kinematic constraint

$$v = \frac{\partial \eta}{\partial t} + u \frac{\partial \eta}{\partial x} \quad \text{on } y = \eta(x, t), \tag{2.4}$$

since by definition fluid may not cross this surface. It is also necessary to satisfy the dynamic condition that the fluid pressure at the interface must equal the air pressure there, and from Bernoulli's equation in the fluid it therefore follows that

$$\frac{\partial \phi}{\partial t} + \tfrac{1}{2}\left(u^2 + v^2\right) + \eta = 0 \quad \text{on } y = \eta(x, t). \tag{2.5}$$

Following Frandsen [4], Hermann and Timokha [2] and Faltinsen et al. [21], it is now convenient to transform the problem to a new non-inertial coordinate system (X, y) with its origin fixed on the moving left wall of the tank. This situation is illustrated in Fig. 1. The required transformation is accomplished by defining the horizontal coordinate

$$X = x - \epsilon \sin t \tag{2.6}$$

and making use of the chain rule of calculus. It is also useful to define a perturbation potential $\hat{\Phi}$ from the original velocity potential ϕ by means of the equation

$$\phi(X, y, t) = \epsilon X \cos t + \hat{\Phi}(X, y, t). \tag{2.7}$$

It follows that the perturbation potential in (2.7) still satisfies Laplace's equation

$$\frac{\partial^2 \hat{\Phi}}{\partial X^2} + \frac{\partial^2 \hat{\Phi}}{\partial y^2} = 0 \quad \text{in } 0 < X < \lambda, \quad -\beta < y < \eta(X, t) \tag{2.8}$$

in the non-inertial coordinate X in (2.6). The bottom condition (2.2) takes the form

$$\frac{\partial \hat{\Phi}}{\partial y} = 0 \quad \text{on } y = -\beta \tag{2.9}$$

and the two tank side conditions (2.3) become simply

$$\frac{\partial \hat{\Phi}}{\partial X} = 0 \quad \text{on } X = 0, \quad X = \lambda. \tag{2.10}$$

The interfacial kinematic condition (2.4) becomes

$$\frac{\partial \hat{\Phi}}{\partial y} = \frac{\partial \eta}{\partial t} + \frac{\partial \hat{\Phi}}{\partial X} \frac{\partial \eta}{\partial X} \quad \text{on } y = \eta(X, t), \tag{2.11}$$

and the dynamic condition (2.5) transforms to

$$-\tfrac{1}{2}\epsilon^2 \cos^2 t - \epsilon X \sin t + \frac{\partial \hat{\Phi}}{\partial t} + \frac{1}{2}\left[\left(\frac{\partial \hat{\Phi}}{\partial X}\right)^2 + \left(\frac{\partial \hat{\Phi}}{\partial y}\right)^2\right] + \eta = 0 \quad \text{on } y = \eta(x, t) \tag{2.12}$$

on the interface.

A solution to this nonlinear free-surface problem thus consists of finding the perturbation potential $\hat{\Phi}(X, y, t)$ and the time-dependent surface elevation $\eta(X, t)$ that satisfy the system of equations (2.8–2.12), at appropriate values of the dimensionless parameters (2.1). A spectral method is outlined in the next section for determining this solution in the non-inertial coordinate system (2.6).

3 The basic spectral method

It follows at once from Laplace's equation (2.8) and the bottom and side conditions (2.9) and (2.10) that the perturbation potential in the fluid may be represented in the form

$$\hat{\Phi}(X, y, t) = P_0(t) + \sum_{m=1}^{M} P_m(t) \frac{\cosh(\alpha_m(y + \beta))}{\cosh(\alpha_m \beta)} \sin\left(\alpha_m\left(X - \frac{\lambda}{2}\right)\right), \tag{3.1}$$

where the constants

$$\alpha_m = (2m - 1)\pi/\lambda \tag{3.2}$$

have been defined for convenience. The hyperbolic cosine term in the denominator of (3.1) has been included so that the Fourier coefficients $P_m(t)$ are quantities of order one, at least for low orders m. This is necessary to avoid ill-conditioning in the numerical algorithm to follow. The interfacial elevation may similarly be expressed as

$$\eta(X, t) = B_0(t) + \sum_{m=1}^{M} B_m(t) \sin\left(\alpha_m\left(X - \frac{\lambda}{2}\right)\right), \tag{3.3}$$

with constants α_m again given by (3.2). Since only derivatives of the potential are actually required, the initial coefficient $P_0(t)$ remains arbitrary, and it is therefore ignored henceforth. The upper limit M of the sums in equations (3.1) and (3.3) is chosen to be as large as possible.

The solution of this free-surface problem has now been reduced to finding the time-dependent Fourier coefficients $P_m(t)$ and $B_m(t)$. We use the approach developed by Forbes et al. [24] to derive a system of ordinary differential equations for these functions. It is convenient to define perturbation velocity components,

$$\hat{U}(X, t) = \frac{\partial \hat{\Phi}}{\partial X} = \sum_{m=1}^{M} \alpha_m P_m(t) \frac{\cosh(\alpha_m(\eta + \beta))}{\cosh(\alpha_m \beta)} \cos\left(\alpha_m\left(X - \frac{\lambda}{2}\right)\right),$$
$$\hat{V}(X, t) = \frac{\partial \hat{\Phi}}{\partial y} = \sum_{m=1}^{M} \alpha_m P_m(t) \frac{\sinh(\alpha_m(\eta + \beta))}{\cosh(\alpha_m \beta)} \sin\left(\alpha_m\left(X - \frac{\lambda}{2}\right)\right), \tag{3.4}$$

along the interface $y = \eta(X, t)$, and these functions will be used extensively in the following developments.

The contribution to the zeroth-order Fourier mode in the kinematic condition (2.11) is obtained by integrating the equation over the tank length. Using integration by parts and (3.4) then gives the simple result

$$B_0'(t) = 0. \tag{3.5}$$

It follows that the Fourier coefficient $B_0(t)$ in (3.3) is constant; if the motion is regarded as having started from rest, then its value may be taken to be zero. As with the problem studied by Forbes et al. [24], it is straightforward to show that (3.5) yields to the fact that the average interface elevation must remain constant, independently of time, as is required by conservation of mass.

The contribution from higher-order Fourier modes in the kinematic condition (2.11) is determined by multiplying by the basis functions $\sin(\alpha_k(X - \lambda/2))$, $k = 1, 2, \ldots, M$ and integrating over the tank length. Integration by parts yields the identity

$$\int_0^\lambda \hat{U} \frac{\partial \eta}{\partial X} \sin\left(\alpha_k \left(X - \frac{\lambda}{2}\right)\right) \mathrm{d}X = \int_0^\lambda \hat{V} \sin\left(\alpha_k \left(X - \frac{\lambda}{2}\right)\right) \mathrm{d}X - \alpha_k \sum_{m=1}^M S_{km} P_m(t), \tag{3.6}$$

after use has been made of the perturbation velocity components (3.4) evaluated on the free surface. The intermediate functions on the right-hand side of (3.6) are defined as

$$S_{km}(t) = \int_0^\lambda \frac{\sinh(\alpha_m(\eta + \beta))}{\cosh(\alpha_m \beta)} \cos\left(\alpha_m \left(X - \frac{\lambda}{2}\right)\right) \cos\left(\alpha_k \left(X - \frac{\lambda}{2}\right)\right) \mathrm{d}X. \tag{3.7}$$

In view of the identity (3.6), the decomposition of the kinematic equation (2.11) into higher Fourier modes yields

$$B_k'(t) = \frac{2\alpha_k}{\lambda} \sum_{m=1}^M S_{km} P_m(t) \quad k = 1, 2, \ldots, M. \tag{3.8}$$

The dynamic surface condition (2.12) is similarly subjected to Fourier decomposition. The zeroth-order mode is obtained simply by integration over the tank length, and yields a differential equation from which the derivative $P_0'(t)$ of the zeroth-order coefficient in (3.1) can be determined. However, as this quantity is never needed, it can be set to zero and the Fourier decomposition at zeroth order can simply be ignored.

Higher-order modes are obtained as previously, multiplying by the same basis functions $\sin(\alpha_k(X - \lambda/2))$, $k = 1, 2, \ldots, M$ and integrating over the interval $X \in (0, \lambda)$. After some algebra, the system of ordinary differential equations

$$\sum_{m=1}^M G_{km} P_m'(t) = -\frac{2\epsilon}{\alpha_k^2} \sin t \cos(k\pi) - \tfrac{1}{2} J_k(t) - \tfrac{1}{2}\lambda B_k(t), \quad k = 1, 2, \ldots, M, \tag{3.9}$$

is obtained, in which the further intermediate quantities,

$$\begin{aligned} G_{km}(t) &= \int_0^\lambda \frac{\cosh(\alpha_m(\eta + \beta))}{\cosh(\alpha_m \beta)} \sin\left(\alpha_m \left(X - \frac{\lambda}{2}\right)\right) \sin\left(\alpha_k \left(X - \frac{\lambda}{2}\right)\right) \mathrm{d}X, \\ J_k(t) &= \int_0^\lambda [\hat{U}^2 + \hat{V}^2] \sin\left(\alpha_k (X - \frac{\lambda}{2})\right) \mathrm{d}X, \end{aligned} \tag{3.10}$$

have been defined for convenience.

Equations 3.8 and 3.9 constitute a system of $2M$ differential equations for the coefficients $P_m(t)$ and $B_m(t)$, $m = 1, 2, \ldots, M$. This system is non-autonomous, but is instead sinusoidally forced, as is evident from the presence of the term involving the function $\sin t$ on the right-hand side of (3.9). Nevertheless, the system is easily solved numerically, and we use the standard fourth-order Runge–Kutta method outlined by Atkinson [26, p. 371] to perform this task. The integrals in (3.7) and (3.10) are evaluated to very high-order accuracy using the composite trapezoidal rule, since their integrands are periodic; see [26, p. 253]. Accurate solutions are generated using $M = 51$ Fourier modes, 201 spatial grid points to evaluate the integrals (3.7) and (3.10), and 151 time steps over each half forcing period $t \in [0, \pi]$.

4 Time-periodic solutions and their stability

Many investigators, including Ockendon and Ockendon [7], Hill [9] and Hill and Frandsen [10], for example, have focussed on the periodic response of the interface to the sinusoidal forcing of the tank. This is able to be determined here, in the fully nonlinear case, based on the algorithm presented in Sect. 3.

The most successful method involves an expansion of each time-dependent Fourier coefficient in a further Fourier series in time. If period Q solutions are sought, with response period $2\pi Q$, then the symmetries of (3.8) and (3.9) permit the additional Fourier expansions to take the forms

$$
P_m(t) = \sum_{n=1}^{N} P_{mn} \cos\left(\frac{(2n-1)t}{Q}\right),
$$

$$
B_m(t) = \sum_{n=1}^{N} B_{mn} \sin\left(\frac{(2n-1)t}{Q}\right) \quad m = 1, 2, \ldots, M.
$$

(4.1)

An unknown vector $\mathbf{u}$ of length $2MN$ is now created, containing the (constant) coefficients B_{mn} and P_{mn} in (4.1). The system of $2MN$ nonlinear equations satisfied by these coefficients is found using Fourier decomposition in time, and may be written

$$
\int_0^{2\pi Q} \mathcal{F}_k \cos\left(\frac{(2n-1)t}{Q}\right) dt = 0, \quad \int_0^{2\pi Q} \mathcal{G}_k \sin\left(\frac{(2n-1)t}{Q}\right) dt = 0, \quad k = 1, 2, \ldots, M, \quad n = 1, 2, \ldots, N.
$$

(4.2)

The quantities in the integrands of (4.2) are obtained from the governing differential equations (3.8) and (3.9), and are given by the expressions

$$
\mathcal{F}_k = B_k'(t) - \frac{2\alpha_k}{\lambda} \sum_{m=1}^{M} S_{km} P_m(t),
$$

$$
\mathcal{G}_k = \sum_{m=1}^{M} G_{km} P_m'(t) + \frac{2\epsilon}{\alpha_k^2} \sin t \cos(k\pi) + \tfrac{1}{2} J_k(t) + \tfrac{1}{2}\lambda B_k(t),
$$

(4.3)

in which the intermediate expressions are as defined in (3.7) and (3.10).

The unknown vector $\mathbf{u}$ containing the $2MN$ coefficients B_{mn} and P_{mn} is updated iteratively, using Newton's method to satisfy the system (4.2) of $2MN$ equations. The integrals in time are evaluated by the composite trapezoidal rule, since it is exponentially accurate for the time-periodic integrands in (4.2). Nevertheless, the Newton algorithm is demanding of computer time, since the integrands (4.3) involve significant effort to evaluate. The advantage, however, is that multiple solution branches and even unstable periodic behaviour can be obtained by this very general approach.

The response amplitude A_T of the nonlinear time-periodic solutions is defined in this paper by the relation

$$
A_T^2 = \frac{2}{\pi Q \lambda} \int_0^{2\pi Q} dt \int_0^{\lambda} dX \, \eta^2(X, t).
$$

(4.4)

When use is made of the expression (3.3) with $B_0 = 0$ and the representation (4.1), the definition (4.4) gives rise to

$$
A_T = \sqrt{\sum_{m=1}^{M} \sum_{n=1}^{N} (B_{mn})^2},
$$

(4.5)

after some calculation. This expression (4.5) is easily evaluated using the coefficients computed from Newton's method of solution.

Once these time-periodic orbits have thus been found by Newton's method, their stability can be assessed relatively easily. Here, a periodic solution is stable if small perturbations decay with time, but unstable if those perturbations grow. The combined set of differential equations (3.8) and (3.9) may be regarded as a non-autonomous dynamical system of the form

$$
\mathbf{V}' = \mathbf{F}(t, \mathbf{V}),
$$

(4.6)

involving the $2M \times 1$ vector of coefficients

$$
\mathbf{V}(t) = \left[B_1(t), \ldots, B_M(t); P_1(t), \ldots, P_M(t) \right]^T.
$$

(4.7)

If the system of equations (4.6) is integrated over one response period $t \in [0, 2\pi Q]$, using an initial vector $\mathbf{V}(0)$ in (4.7) computed from the coefficients obtained with Newton's method above, then the same vector $\mathbf{V}(2\pi Q) = \mathbf{V}(0)$ will be obtained at time $t = 2\pi Q$, because of the periodicity of the solution (4.1). However, suppose that a new initial vector $\mathbf{V}_j(0)$ is created by adding a small quantity ξ to the j-th component of $\mathbf{V}(0)$. In component form, this may be denoted as $(V_j)_i(0) = V_i(0) + \xi \delta_{ij}$ in which δ_{ij} is the Kronecker delta symbol that has the value 0 if $i \neq j$ and 1 if $i = j$. If this new perturbed vector is used as the initial condition for the system (4.6) and integrated over a period, some new vector $\mathbf{V}_j(2\pi Q)$ will result. In general, it will differ from the perturbed initial vector, and the extent to which it does so is a measure of the stability of the solution. This process is repeated for each component $j = 1, 2, \ldots, 2M$ and used to create the $2M \times 2M$ matrix $\mathbf{M}$ with components

$$M_{ij} = \frac{(V_j)_i(2\pi Q) - (V_j)_i(0)}{\xi}, \quad i, j = 1, 2, \ldots, 2M. \tag{4.8}$$

It may be shown that the matrix $\mathbf{M}$ is the *monodromy matrix* of Floquet theory, if ξ is sufficiently small (strictly, $\xi \to 0$ in (4.8)), as is detailed by Seydel [8, p. 255]. The eigenvalues of $\mathbf{M}$ determine the stability of the periodic solution computed by Newton's method. If all eigenvalues have absolute value less than or equal to one, then the solution is stable; however, the solution becomes unstable if the absolute value of any one eigenvalue exceeds one. This is portrayed very conveniently in graphical form, since eigenvalues of unit absolute value all lie on a circle of unit radius in the complex plane. Stable solutions are those for which all the eigenvalues lie within or on the unit circle, and if any eigenvalue leaves the circle, then the solution becomes unstable.

5 Linear and weakly nonlinear theories

The linearized approximation to the problem presented in Sect. 2 is derived by assuming that the perturbation potential and the interface elevation can be expanded in powers of the forcing amplitude in the form

$$\hat{\Phi}(X, y, t) = \epsilon \hat{\Phi}_1(X, y, t) + \mathcal{O}(\epsilon^2), \quad \eta(X, t) = \epsilon H_1(X, t) + \mathcal{O}(\epsilon^2). \tag{5.1}$$

These expansions (5.1) are substituted in the governing equations and terms are retained to the first order in ϵ.

It is found that the linearized perturbation potential $\hat{\Phi}_1$ satisfies Laplace's equation (2.8), although now in the rectangular linearized fluid region $0 < X < \lambda$, $-\beta < y < 0$. This potential also obeys the required conditions (2.9), (2.10) on the tank boundaries. The linearized kinematic condition (2.11) becomes

$$\frac{\partial \hat{\Phi}_1}{\partial y} = \frac{\partial H_1}{\partial t} \quad \text{on } y = 0 \tag{5.2}$$

to the first order in ϵ, and the corresponding linearized equivalent of the dynamic condition (2.12) is

$$-X \sin t + \frac{\partial \hat{\Phi}_1}{\partial t} + H_1 = 0 \quad \text{on } y = 0. \tag{5.3}$$

The solution to this linearized system of equations, subject to the conditions (5.2) and (5.3) on the linearized surface $y = 0$, is found in a straightforward manner using separation of variables. As the forcing term is periodic in time, with period 2π, the appropriate periodic solution is

$$\hat{\Phi}(X, y, t) = \epsilon \cos t \sum_{m=1}^{\infty} P_m^L \frac{\cosh(\alpha_m(y + \beta))}{\cosh(\alpha_m \beta)} \sin\left(\alpha_m\left(X - \frac{\lambda}{2}\right)\right) + \mathcal{O}(\epsilon^2),$$

$$\eta(X, t) = \epsilon \sin t \sum_{m=1}^{\infty} B_m^L \sin\left(\alpha_m\left(X - \frac{\lambda}{2}\right)\right) + \mathcal{O}(\epsilon^2), \tag{5.4}$$

corresponding to the forms (3.1) and (3.3) assumed for the nonlinear solution. The linearized coefficients in (5.4) are found to be

$$P_m^L = -\frac{4\cos(m\pi)\cosh(\alpha_m \beta)}{\alpha_m^2 \lambda[\alpha_m \sinh(\alpha_m \beta) - \cosh(\alpha_m \beta)]}, \quad B_m^L = -\frac{4\cos(m\pi)\sinh(\alpha_m \beta)}{\alpha_m^2 \lambda[\alpha_m \sinh(\alpha_m \beta) - \cosh(\alpha_m \beta)]}, \tag{5.5}$$

where the constants α_m are as given in (3.2). It follows from the definition (4.4) that the linearized amplitude of the surface disturbance is

$$A_T = \epsilon \sqrt{\sum_{m=1}^{\infty} \left(B_m^L\right)^2} \tag{5.6}$$

and this forms a valuable point of comparison with the results (4.5) of the fully nonlinear solution.

The linearized solution (5.4), (5.5) shows that resonances occur whenever

$$\tanh(\alpha_m \beta) = \frac{1}{\alpha_m}. \tag{5.7}$$

This is effectively a transcendental equation for the quantity α_m in (3.2), and has a unique solution for each value of the integer m. If the tank is very deep, so that $\beta \to \infty$, then Eq. (5.7) shows that resonances occur at the values $\lambda \to (2m - 1)\pi$ of the tank length, in these dimensionless variables.

Since linearized theory is only valid for small response amplitudes, it is necessarily the case that the solution (5.4), (5.5) fails for parameter values close to the resonances (5.7). Consequently, Ockendon and Ockendon [7], Hill [9] and Hill and Frandsen [10] have developed weakly nonlinear theories appropriate to the solution near the first resonance (at which $m = 1$ in (5.7)). For completeness, a similar analysis is now presented here, and is relatively straightforward to perform, in view of the particularly simple form of the ordinary differential equations (3.8) and (3.9) in the Fourier space, derived in this present formulation.

The interface elevation function in (3.3) is approximated by the monochromatic term

$$\eta(X, t) \approx B_{11} \sin t \sin\left(\alpha_1 \left(X - \frac{\lambda}{2}\right)\right) = -B_{11} \sin t \cos(\pi X / \lambda). \tag{5.8}$$

This form (5.8) is now substituted directly in the governing differential equations in Sect. 3. After some calculation, and when use is made of an integral identity from [27, Eq. 3.997.2] the intermediate quantity of interest in (3.7) becomes

$$S_{11}(t) = \lambda \tanh\left(\frac{\pi \beta}{\lambda}\right) \frac{I_1(T)}{T}, \tag{5.9}$$

in which I_1 denotes the modified first-kind Bessel function of first order. It is similarly appropriate to approximate the perturbation potential (3.1) with the single term

$$\hat{\Phi}(X, y, t) \approx P_{11} \cos t \frac{\cosh(\alpha_1(y + \beta))}{\cosh(\alpha_1 \beta)} \sin\left(\alpha_1 \left(X - \frac{\lambda}{2}\right)\right). \tag{5.10}$$

The perturbation velocity components $\hat{U}$ and $\hat{V}$ in (3.4) are evaluated without further approximation using (5.10) and (5.8). The relevant intermediate quantities in (3.10) are then obtained in the forms

$$G_{11}(t) = \lambda \left[I_0(T) - \frac{I_1(T)}{T}\right], \quad J_1(t) = \frac{\pi^2}{\lambda} \cos^2 t \, (P_{11})^2 \tanh\left(\frac{\pi \beta}{\lambda}\right) I_1(2T), \tag{5.11}$$

after somewhat extensive algebra. The quantity T in (5.9) and (5.11) is defined for convenience as

$$T = \frac{\pi}{\lambda} B_{11} \sin t, \tag{5.12}$$

and the symbols I_ν, $\nu = 0, 1$, denote the modified Bessel function of the first kind, of order ν.
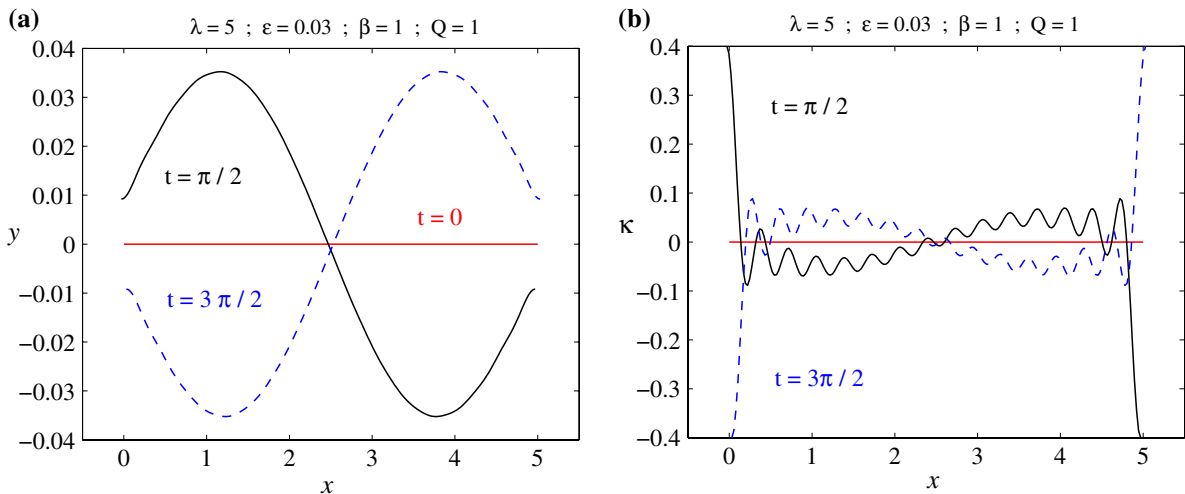
It is sufficient for the present approximation to make use of the results

$$I_0(T) = 1 + \mathcal{O}(T^2), \quad I_1(T) = T/2 + \mathcal{O}(T^3)$$

for the modified Bessel functions, taken from [28, p. 375]. When these expressions are used in (5.9) and (5.11) and only the terms of the same period 2π as the forcing term are retained, the governing ordinary differential equations (3.8) and (3.9) become approximately

$$B_{11} \cos t \approx \frac{\pi}{\lambda} P_{11} \tanh\left(\frac{\pi \beta}{\lambda}\right) \cos t,$$

$$-\frac{\lambda}{2} P_{11} \sin t \approx \left[\frac{2\lambda^2 \epsilon}{\pi^2} - \frac{\pi^3}{8\lambda^2} (P_{11})^2 B_{11} \tanh\left(\frac{\pi \beta}{\lambda}\right) - \frac{\lambda}{2} B_{11}\right] \sin t. \tag{5.13}$$

Fig. 2 **a** Surface profiles and **b** Surface curvatures, for a 2π-periodic solution obtained with $\lambda = 5$, $\beta = 1$ and forcing amplitude $\epsilon = 0.03$. Solutions are shown for the three times $t = 0$, $\pi/2$ and $3\pi/2$

Eliminating the constant P_{11} in the system (5.13) gives rise to the cubic equation

$$(B_{11})^3 + \frac{4\lambda}{\pi}\left[\tanh\left(\frac{\pi\beta}{\lambda}\right) - \frac{\lambda}{\pi}\right]B_{11} - \epsilon\frac{16\lambda^2}{\pi^3}\tanh\left(\frac{\pi\beta}{\lambda}\right) \approx 0 \tag{5.14}$$

for the coefficient B_{11} in (5.8). Observe that the definition (4.4) gives the surface amplitude at this order of approximation to be $A_T \approx |B_{11}|$, precisely as expected. The cubic (5.14) has either one or three real roots, and predicts multiple solutions in an interval of tank lengths λ slightly greater than the resonant length obtained from (5.7) with $m = 1$. On a plot of response amplitude A_T against tank length λ, the weakly nonlinear solution (5.8), (5.14) therefore predicts a resonance peak bending in the direction of increasing λ, as will be seen in Sect. 6. This is a resonance peak of the "hardening spring" type; see [8, p. 53].

This weakly nonlinear analysis can be repeated for the other resonances. Near the second resonance, obtained with $m = 2$ in (5.7), it is appropriate to seek a solution of the form

$$\eta(X, t) \approx B_{21} \sin t \cos(3\pi X/\lambda), \tag{5.15}$$

and after a similar analysis to that above, it is found that the response amplitude B_{21} satisfies the cubic equation

$$(B_{21})^3 + \frac{4\lambda}{3\pi}\left[\tanh\left(\frac{3\pi\beta}{\lambda}\right) - \frac{\lambda}{3\pi}\right]B_{21} + \epsilon\frac{16\lambda^2}{27\pi^3}\tanh\left(\frac{3\pi\beta}{\lambda}\right) \approx 0. \tag{5.16}$$

This analysis predicts a resonance peak bending in the direction of the positive λ-axis, similarly to the result (5.14) for the first resonance.

6 Presentation of results

This discussion of results begins with a consideration of a time-periodic solution of period 2π, so that $Q = 1$ in (4.1) in Sect. 4. Figure 2 illustrates the behaviour of the free surface as a function of time, for a tank of depth $\beta = 1$ and length $\lambda = 5$, subjected to horizontal forcing of amplitude $\epsilon = 0.03$.

The free-surface profiles are shown in Fig. 2a at the three times $t = 0$, $\pi/2$ and $3\pi/2$ in the original inertial reference coordinates (x, y). As the solution is periodic, the surface profile at $t = \pi$ is identical to the situation for $t = 0$ and 2π, after which the cycle simply repeats. The profiles in Fig. 2 are solutions to the full nonlinear equations, but are nevertheless in close agreement with the predictions of the linearized theory (5.4), (5.5), since
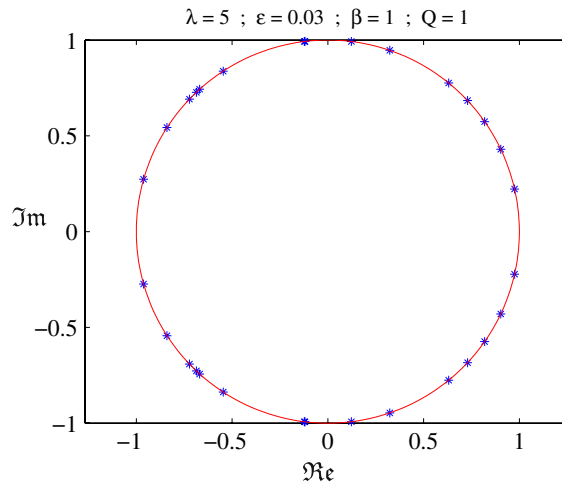
this value of tank length $\lambda = 5$ is far from resonance. The solution at time $t = 3\pi/2$ is essentially the mirror image of the profile at $t = \pi/2$, although translated slightly to the right due to the horizontal motion of the tank, which is visible in these stationary coordinates.

There is, however, one feature of the nonlinear results in Fig. 2 that is not present in the linearized approximation; at the tank walls $X = 0$ and $X = \lambda$, the free surface develops very high curvature. This feature may be visible from the profiles in Fig. 2a, but is easily seen in Fig. 2b. Here, the curvature,

$$\kappa = \frac{\eta_{XX}}{\left[1 + \eta_X^2\right]^{3/2}}, \tag{6.1}$$

at the free surface has been computed from the spectral representation (3.3) and is shown in Fig. 2b at the same three times $t = 0$, $\pi/2$ and $3\pi/2$. There is an inflexion point at about the centre of the tank, at which the curvature κ in (6.1) changes sign, but the main feature of the diagram are the large spikes in curvature that form at each tank wall. It is a strength of the present numerical scheme that accurate values of curvature may be computed, using exact differentiation of the surface elevation (3.3); nevertheless, in this case, the curvature spikes at each tank wall pose difficulties for the convergence of the Fourier series (3.3), and have resulted in the small oscillations in the curvature profile that are visible in Fig. 2b. This is evidence of Gibbs' phenomenon; see [29, p. 510]. As the number of Fourier modes in this numerical solution is increased, the sizes of the spikes in curvature remain largely unaffected, although the frequency of the oscillations caused by Gibbs' phenomenon increases, and the amplitude of most of these waves is diminished. These small oscillations in curvature are therefore not representative of the exact physics, but rather are a consequence of the numerical solution technique. Indeed, any approximation method for which the error can be represented as a Fourier series can be expected to produce similar oscillations when computing these curvature spikes.

The stability of the periodic forced solutions in Fig. 2 can be assessed using the analysis of Sect. 4, based on Floquet theory. The eigenvalues of the monodromy matrix (4.8) have been computed for this case, and are shown in the complex eigenvalue plane in Fig. 3. This solution was obtained with $M = 15$ spatial modes and $N = 10$ temporal harmonics, so that the matrix **M** in equation (4.8) has $2M = 30$ eigenvalues. These all have unit absolute value (within an error of 0.07%). They are therefore distributed around the circle of unit radius in the complex plane, and this is also shown in Fig. 3 with a thin solid line. The periodic solution of Fig. 2 is therefore stable in the sense that small perturbations to it will not grow in time. In fact, since the eigenvalues all have magnitude equal to one, then the solution is neutrally stable, and so represents a travelling wave, as is to be expected on physical grounds.

Although the periodic response shown in Fig. 2 is stable to small perturbations, it is nevertheless of interest to consider the behaviour of the free-surface when the solution is started from a flat interface at rest. This can be

(a)

(b)
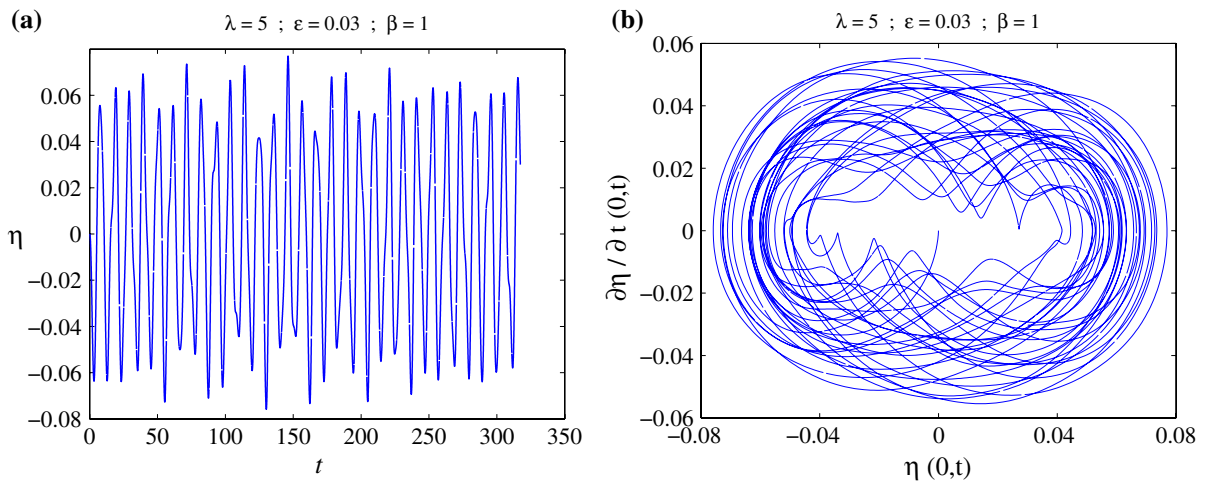
Fig. 4 **a** Free-surface profile at the left wall as a function of time, and **b** Phase-plane diagram for surface height at the left wall. Results are shown for a solution started from rest, for the case $\lambda = 5$, $\beta = 1$ and forcing amplitude $\epsilon = 0.03$

determined easily in the present spectral formulation, simply by integrating the ordinary differential equations (3.8) and (3.9). The results are shown for this same case in Fig. 4. Here, $M = 51$ spatial modes were used, and the solution has been integrated over the interval $t \in [0, 101\pi]$, representing about 50 forcing periods.

Figure 4a shows the free-surface elevation η at the left-hand edge $X = 0$ of the tank. The motion is clearly irregular in both amplitude and phase, and there is no evidence of any approach to the (stable) periodic solution shown in Fig. 2. As a check, Fig. 4b shows a type of phase-plane plot for this solution, made up of the time derivative of the surface height at the left edge of the tank plotted against the height. The irregular and non-repeating nature of this diagram shows that the pattern of behaviour is either quasi-periodic or even fully chaotic in time. This point is considered again, later in this section. Somewhat similar diagrams to those of Fig. 4 have also been presented by Frandsen [4] using a finite-difference approach to the nonlinear problem. These results show that, while the time-periodic solution in Fig. 2 is stable, it may nevertheless not be the outcome that is actually observed, depending on the starting conditions in the tank.

The time-periodic response of the free surface is analyzed in detail in Fig. 5. Here, the response amplitude is plotted against the tank length λ, for the case of a tank of depth $\beta = 1$ subjected to forcing oscillations of amplitude $\epsilon = 0.03$. The results in Fig. 5 in some sense represent the major focus of this paper, and were obtained with 320 separate converged nonlinear periodic solutions at different tank lengths λ, generated using the methods outlined in Sect. 4. Similar results were produced with the larger forcing amplitude $\epsilon = 0.1$, but these will not be discussed here.

The thin solid line in Fig. 5 represents the linearized amplitude computed from (5.5) and (5.6), and 51 Fourier coefficients were found to give highly converged profiles for this solution. The first two resonances at tank lengths $\lambda \approx 2.6187$ and $\lambda \approx 7.8561$ are visible as near-vertical sections in the linearized amplitude curve, as predicted from the result (5.7). The thin dashed lines on this graph correspond to the weakly nonlinear amplitudes $|B_{11}|$ and $|B_{21}|$ at the first and second resonances, computed from the two cubic equations (5.14) and (5.16), respectively. Finally, the thick solid lines represent amplitudes A_T computed from Newton's method solution, for the fully nonlinear problem, using (4.5).

The linearized results give a good description of the nonlinear solution amplitude for small to moderate-sized waves, as is to be expected. Near the first resonance at $\lambda \approx 2.6187$, however, the nonlinear time-periodic solution fails, due to the formation of regions of very high curvature at the wave crests, similar to those shown in Fig. 2b. This strongly suggests that periodic nonlinear solutions are ultimately limited by the formation of points of infinite curvature at the interface, similar to those encountered by Moore [30] and Cowley et al. [31], at least in the vicinity of the first resonance.

The situation near the second resonance at $\lambda \approx 7.8561$ is considerably more interesting. Perhaps the most surprising feature is that the linearized result gives a remarkably accurate description of the nonlinear periodic behaviour, even for large-amplitude solutions. By contrast, the weakly nonlinear solution obtained from (5.16) describes the nonlinear results rather poorly, and is only qualitatively correct in the sense that it predicts that the amplitude curve bends to the right of the figure, producing multiple solutions for tank length λ greater than the second resonance value. This poor agreement is likely to be due to the fact that the weakly nonlinear theory (5.16) comes from a monochromatic representation (5.15), whereas both the linearized and nonlinear solutions make use of all the Fourier modes. There is also a very narrow region of multiple solutions to the left of the second resonance point, since the unstable nonlinear solution branch above the point marked "B" actually bends back slightly to the left, before eventually failing at an amplitude at which the curvature at the free surface becomes extremely large. These portions of the solution branch were computed using a modification to the Newton-method algorithm of Sect. 4, in which the response amplitude A_T was specified in advance and the forcing amplitude ϵ was obtained as an unknown.

To the right of the second resonance, the fully nonlinear solution develops four separate solution branches, and these are visible in Fig. 5. The solution branch with smallest amplitude to the right of the resonance peak is stable, but the other three branches are all unstable. Careful analysis of the Jacobian matrix in Newton's method, in addition to stability considerations of the various solution branches, indicates that the two points labelled "A" and "B" on the figure are points of genuine bifurcation (at which the Jacobian determinant changes sign). This second resonance is therefore considerably more complex in structure than the weakly nonlinear analysis (5.16) allows; it has more in common with the structure shown in Fig. 4 of the paper by Amundsen et al. [13], although that analysis did not predict the bifurcation points. The experimental results shown in [6, Fig. 17] likewise demonstrate comparable behaviour near the second resonance. There is another point slightly to the right of point "B" in Fig. 5 at which the solution branches appear to cross. This, however, is not a bifurcation, since neither the sign of the determinant of the Jacobian nor the stability of the branches changes as this point is traversed.

It is now appropriate to examine in more detail the various periodic nonlinear solutions that have been summarized in Fig. 5. First a branch of solutions is shown in Fig. 6 at the tank length $\lambda = 2$, which represents the solutions at the extreme left hand side of Fig. 5. Here, the amplitude A_T of the nonlinear solution is shown against the forcing amplitude ϵ of the tank oscillations. In this diagram, the tank depth is again $\beta = 1$.
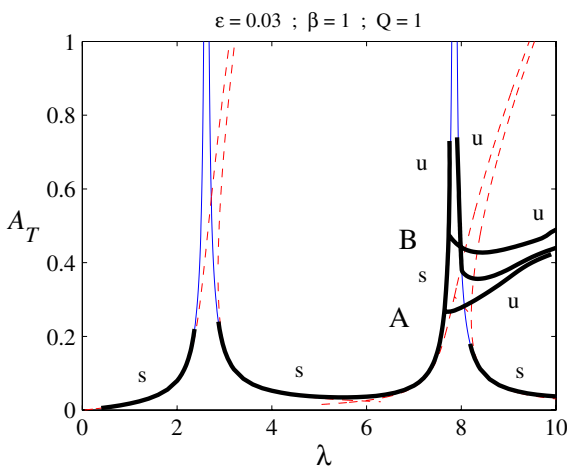
Fig. 5 The dependence of the response amplitude A_T on the tank length λ, for a tank of depth $\beta = 1$ and subject to forcing amplitude $\epsilon = 0.03$. The linearized solution is shown with a *thin solid line*, the *dashed lines* are the predictions of the weakly nonlinear theory, and the *heavy solid line* shows the fully nonlinear solution. Stable solutions are marked "s" and unstable are denoted "u"
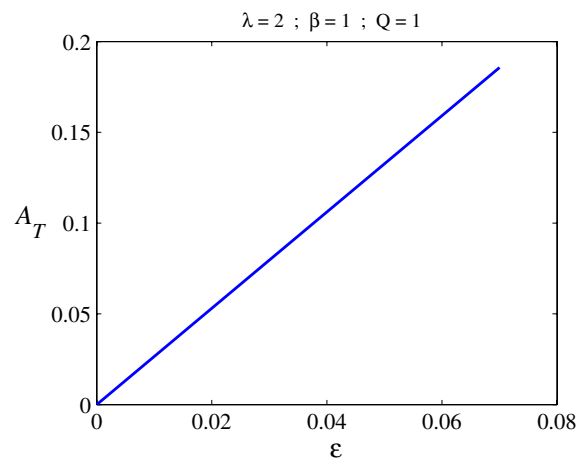
Fig. 6 The dependence of the response amplitude A_T on the forcing amplitude ϵ, for a tank of length $\lambda = 2$ and depth $\beta = 1$

(a)

(b)
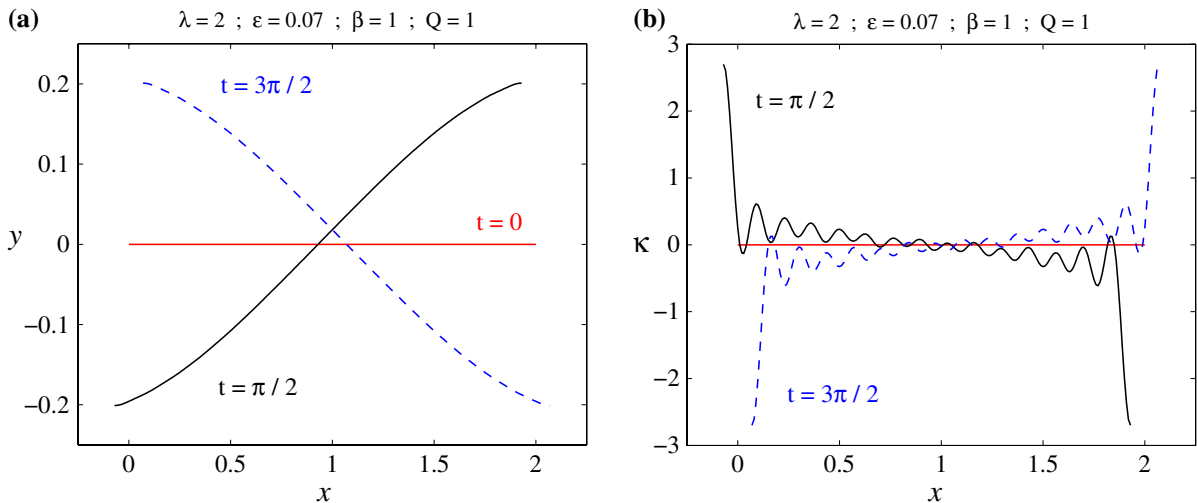
Fig. 7 a Surface profiles and **b** Surface curvatures, for a 2π-periodic solution obtained with $\lambda = 2$, $\beta = 1$ and forcing amplitude $\epsilon = 0.07$. Solutions are shown for the three times $t = 0, \pi/2$ and $3\pi/2$

Figure 6 is at first an unremarkable diagram, as it merely shows that the response amplitude A_T essentially just increases linearly with forcing amplitude ϵ, as might be anticipated from the linearized solution. However, this branch of nonlinear periodic solutions eventually fails at about $\epsilon = 0.07$. In addition, it loses stability at some forcing amplitude at about $\epsilon = 0.04$, so that there is a bifurcation that occurs at this amplitude. These two features of the solution branch in Fig. 6 are now investigated in more detail.

Figure 7a shows the free-surface profile at the three times $t = 0, \pi/2$ and $3\pi/2$, for tank length $\lambda = 2$ and depth $\beta = 1$, at the forcing amplitude $\epsilon = 0.07$. This is, in fact, the largest amplitude to which the solution branch in Fig. 6 could be continued, and attempts to increase it beyond this value were not successful. Clearly some limiting configuration is being approached in this solution, and the Newton algorithm took 63 iterations to converge in this case.

Nevertheless, the solution profiles in Fig. 7a appear unremarkable, and a very similar result is obtained simply using the linearized approximation of Sect. 5. To see the reason for the failure of the solution branch in Fig. 6 at the amplitude $\epsilon = 0.07$ depicted in Fig. 7a, it is necessary to examine the curvature, and this is again computed with good reliability using (6.1) and (3.3). The free-surface curvature is shown for this case in Fig. 7b. Clearly the curvature takes very large values at the two walls at $X = 0$ and $X = \lambda$, and these results strongly suggest that the limiting configuration involves infinite curvature at the tank walls. As with Fig. 2b, there are small spurious oscillations in the curvature profile shown in Fig. 7b, and these are evidence of Gibbs' phenomenon, caused by the presence of the large spikes in curvature at the tank walls.

As indicated previously, the solution branch in Fig. 6 changes from stable at small amplitudes to unstable at larger amplitudes, and this is studied in more detail in Fig. 8. For $\epsilon = 0.03$, as in Fig. 5, the nonlinear periodic solution is stable, and the eigenvalues of the monodromy matrix (4.8) are shown in Fig. 8a. The unit circle is also drawn on this diagram, and it is found that the eigenvalues all lie on this circle to within an error of 0.04%. This represents a very sensitive test on the accuracy of the numerical techniques outlined in this paper, and shows that this solution at $\epsilon = 0.03$ is clearly stable.

By contrast, the solution in Fig. 7 obtained with forcing amplitude $\epsilon = 0.07$ is unstable, and its eigenvalues are shown in Fig. 8b. This diagram gives some insight into the mechanism by which the solution has become unstable, since although most of the eigenvalues of the monodromy matrix are still clustered around the unit circle, a complex conjugate pair has moved beyond the circle. Their absolute values exceed one, and so they are responsible for the instability. Furthermore, the angle at which they exit the unit circle has been monitored, and is not obviously a rational fraction of π radians (the complex conjugate pair of eigenvalues outside the unit circle in Fig. 8b makes

(a) $\lambda = 2$; $\varepsilon = 0.03$; $\beta = 1$; $Q = 1$

(b) $\lambda = 2$; $\varepsilon = 0.07$; $\beta = 1$; $Q = 1$
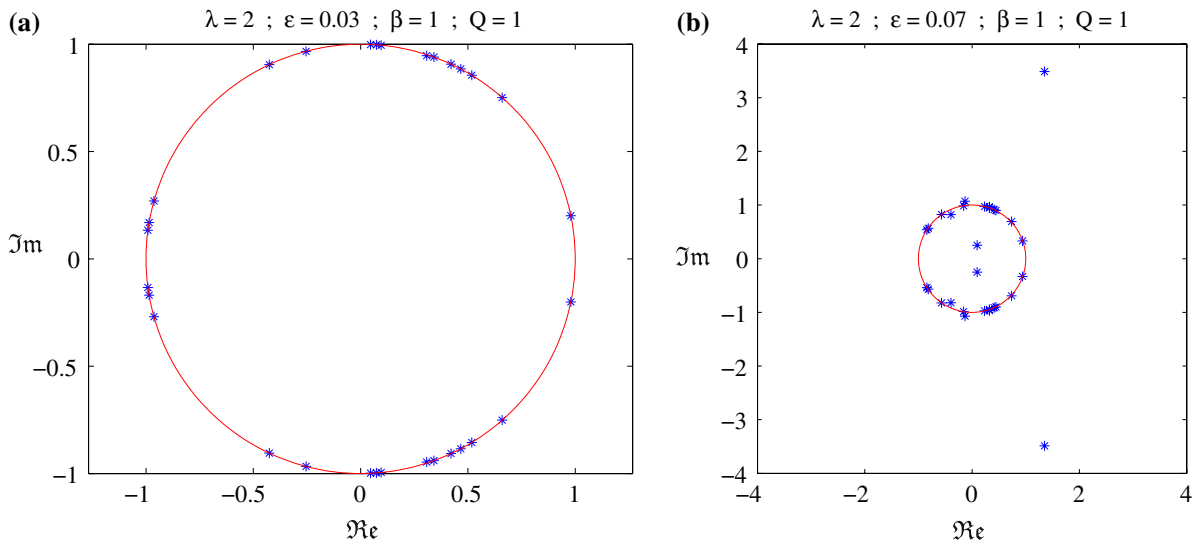
Fig. 8 Eigenvalues of the monodromy matrix (4.8) in the complex plane, for the periodic solution obtained with length $\lambda = 2$ and depth $\beta = 1$, for **a** Forcing amplitude $\epsilon = 0.03$ and **b** Forcing amplitude $\epsilon = 0.07$

an angle $\pi/2.6149$ to the real axis). This strongly suggests that the branch of solutions in Fig. 6 loses its stability at about $\epsilon = 0.04$ through a quasi-periodic bifurcation. Once such a quasi-periodic solution has been produced by this mechanism, it is likely to undergo a further Ruelle–Takens–Newhouse bifurcation to chaos, as outlined for example, by Seydel [8, p. 339]. An example of such irregular solution behaviour has already been encountered in Fig. 4.

The four separate periodic solution branches produced by the second resonance in Fig. 5 are now studied in more detail. Figure 9 shows the response amplitude A_T for these solutions, as functions of the forcing amplitude ϵ, for tank length $\lambda = 9$. The tank depth is again $\beta = 1$. This diagram summarizes the results of 162 separate converged solutions obtained with the Newton algorithm of Sect. 4. In the following discussion, these four solution types will be referred to as Branches 1 to 4, numbered from the bottom of Fig. 5 upwards. Thus the solution at $\lambda = 9$ in Fig. 5 of smallest amplitude is referred to as Branch 1, and it is stable. Its behaviour in Fig. 9 is very similar to the corresponding solution for $\lambda = 2$ shown in Fig. 6; its amplitude increases essentially linearly with forcing amplitude ϵ until it fails at about $\epsilon = 0.122$. For this limiting configuration, the curvature becomes very large at the tank walls. Unlike the situation in Fig. 6, however, the Branch 1 solution in Fig. 9 does not lose its stability as ϵ is increased, but remains stable throughout.

The development of the three unstable solution Branches 2–4 with increasing forcing amplitude ϵ is also shown in Fig. 9. Perhaps the feature of greatest interest is the fact that Branches 2 and 3 are both seen to emerge from the same point $(\epsilon, A_T) = (0, 0.370751)$, indicating that they both bifurcate from the same unstable standing wave solution. The Branch 4 solution (which emanates from the point labelled "B" in Fig. 5) is also seen in Fig. 9 to have arisen from a standing wave solution with $(\epsilon, A_T) = (0, 0.452328)$. Branches 3 and 4 appear to cross over at about $\epsilon = 0.1$ in Fig. 9 since their response amplitudes become equal there. Nevertheless, this is not a genuine bifurcation, since there is no change in sign of the determinant in Newton's method nor any exchange of stability there.

Figure 10 shows the solution profile for the Branch 1 solution at forcing amplitude $\epsilon = 0.03$ and tank length $\lambda = 9$ (as in Fig. 5). The solution is shown at the three times $t = 0$, $\pi/2$ and $3\pi/2$, after which time the pattern simply repeats with 2π-periodicity in time. This is very similar to the corresponding linearized solution at the same parameter values, except for the small regions of moderately high curvature near the tank wall, which may be visible from Fig. 10.

Profiles for the remaining three Branches 2–4 are shown in Fig. 11. Each of these solutions is unstable, as is perhaps to be expected from the small wavelets present in each profile. Analysis of the monodromy matrix shows
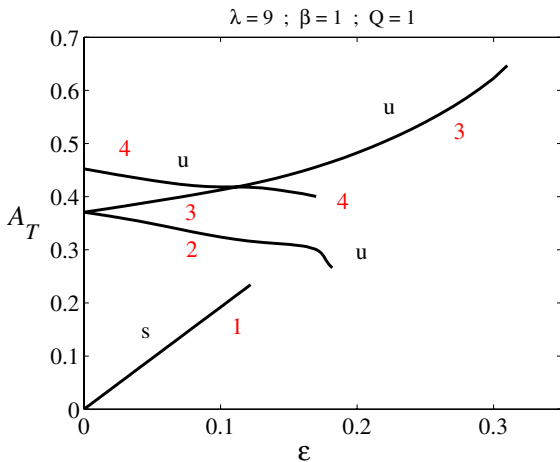
Fig. 9 The dependence of the response amplitude A_T on the forcing amplitude ϵ, for a tank of length $\lambda = 9$ and depth $\beta = 1$. The four different nonlinear branches are shown, and are numbered 1–4 for consistency with Figs. 10 and 11. Stable solutions are marked "s" and unstable are denoted "u"
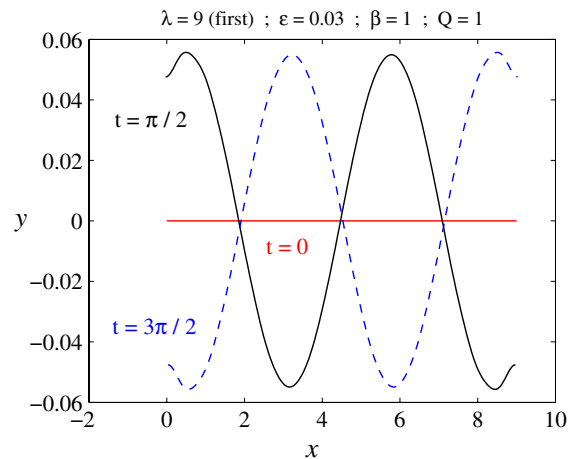
Fig. 10 Surface profiles for Branch 1, for 2π-periodic solutions obtained with $\lambda = 9$, $\beta = 1$ and forcing amplitude $\epsilon = 0.03$. Solutions are shown for the three times $t = 0$, $\pi/2$ and $3\pi/2$

that there is at least one eigenvalue of very large magnitude, so that each of these solutions is so highly unstable that it would not ever be seen in practice. Nevertheless, these periodic solutions are a product of nonlinear behaviour at the second resonance, and it is necessary to compute them in order to understand fully the resonant behaviour of sloshing motion in a tank, such as the abrupt termination of the stable branch of solutions at the point B in Fig. 5.
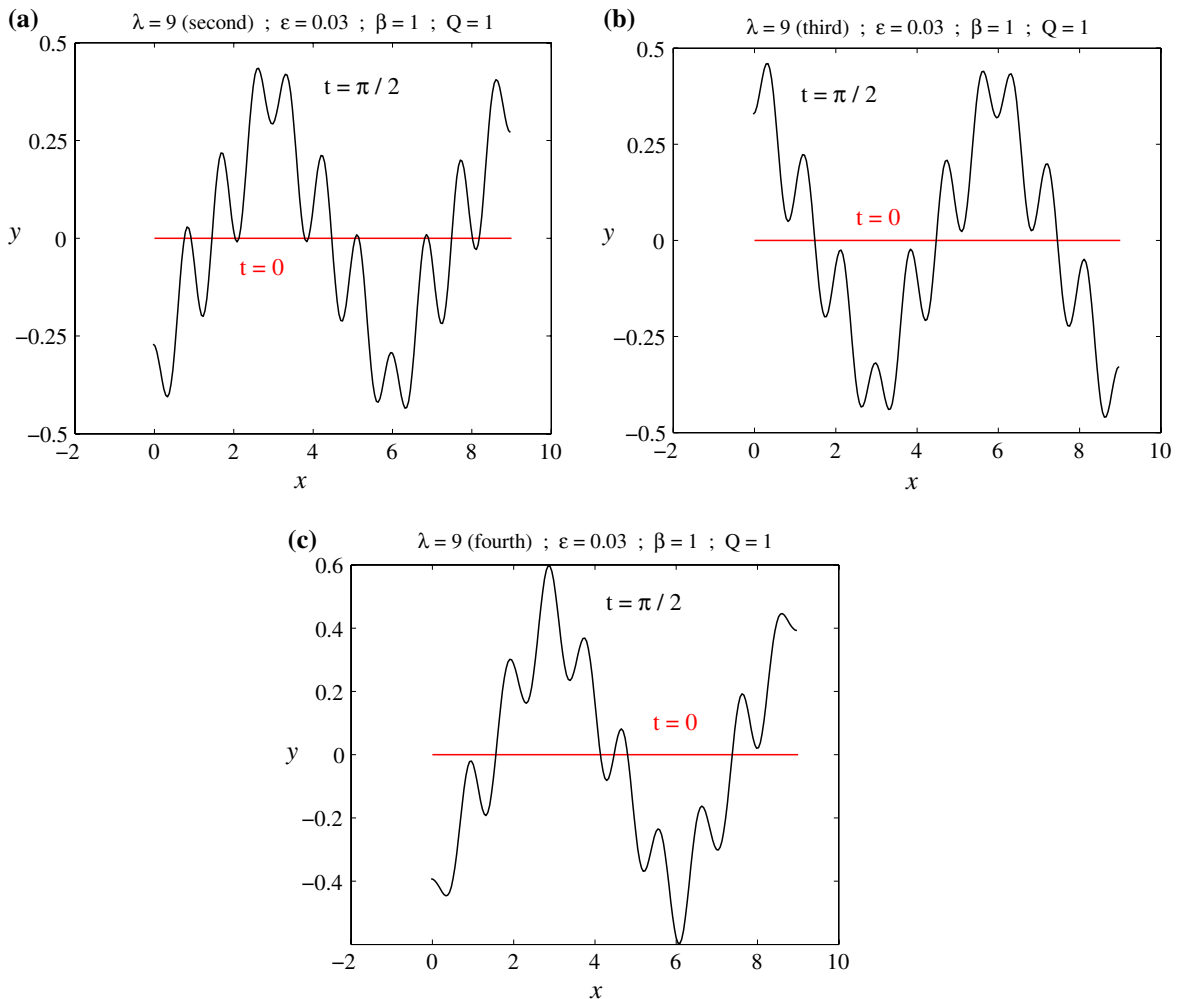
7 Conclusion and discussion

A theoretical analysis of two-dimensional horizontal forcing of a rectangular tank containing an ideal fluid has been presented. A novel spectral method introduced by Forbes et al. [24] has been employed, generalizing the technique of Faltinsen et al. [21]; it allows both irregular time-dependent evolution of the surface and regular periodic solutions to be computed. Stability is determined in this spectral approach using Floquet theory, which also serves as a sensitive check on the accuracy of the solutions computed with this technique. It is found that the nonlinear solutions that correspond to the linearized periodic solutions are neutrally stable, as befits travelling waves. However, the nonlinear resonances may also give rise to other unstable solution branches, so that multiple solutions are possible in certain parameter regions. An example has been presented of four different solutions all at the same parameter values.

The spectral Galerkin approach of the present paper is also well suited to use in the derivation of weakly nonlinear theories. It is found, however, that these give only a poor, qualitative, description of the sloshing behaviour near resonance, presumably since they only make use of one Fourier mode. Fully nonlinear results have been presented for the first two resonances, and the second resonance, in particular, has been shown to have a complex structure not unlike that found experimentally by Chester and Bones [6].

Irregular solutions, as described by Chester and Bones [6] and computed by Frandsen [4], have been obtained here using the present spectral technique. Evidence has been presented that such solutions can arise through quasi-periodic bifurcations from a stable periodic solution, as the forcing amplitude is increased. It is then highly likely that further increases of the amplitude will lead directly to chaos through the mechanism of Ruelle–Takens–Newhouse bifurcation. From a pragmatic point of view, the differences between a quasi-periodic and a fully chaotic solution are not of great significance, since both give free-surface behaviour that is highly irregular. Deciding between these two solution behaviours was therefore not of interest here, but might be determined using Lyapunov exponents or other techniques if desired; this is outside the scope of interest of the present investigation.

(a) $\lambda = 9$ (second) ; $\varepsilon = 0.03$; $\beta = 1$; $Q = 1$

(b) $\lambda = 9$ (third) ; $\varepsilon = 0.03$; $\beta = 1$; $Q = 1$

(c) $\lambda = 9$ (fourth) ; $\varepsilon = 0.03$; $\beta = 1$; $Q = 1$

Fig. 11 Surface profiles for **a** Branch 2, **b** Branch 3 and **c** Branch 4, for 2π-periodic solutions obtained with $\lambda = 9$, $\beta = 1$ and forcing amplitude $\epsilon = 0.03$. Solutions are shown for the two times $t = 0$ and $\pi/2$

As viscosity has been ignored in these solutions, it is found that the various solution branches are often limited by the formation of points of infinite curvature at the interface. This usually occurs at the tank walls. A further advantage of this novel spectral technique is that it allows curvature, normally a difficult quantity to compute, to be obtained in a straightforward manner, and usually with high accuracy. Near the limiting solution configurations, when curvature becomes very large at selected points, small oscillations appear in the curvature profiles, as a manifestation of Gibbs' phenomenon. These inviscid curvature singularities are known in other contexts through the work of Moore [30] and Cowley et al. [31], for example. They occur near the first resonance, preventing the nonlinear solution from exhibiting the exotic behaviour observed at the second resonance. In an attempt to explore the structure of the first resonance, surface tension was added into the formulation of the problem, but was not found to make any significant difference to the results, and so has not been discussed in this paper. Future work that includes the effects of viscosity may possibly show that these points of large curvature in the inviscid problem could trigger over-turning of the free surface in the viscous case, similar to the situation that occurs with the Rayleigh–Taylor instability [32].

Period-doubled and higher-period solutions have been sought with this technique, and in principle can be computed simply by choosing the integer $Q > 1$ in (4.1). Obtaining such solutions, however, is a somewhat serendipitous

affair, as it relies on having an initial guess in the Newton method algorithm that can give convergence to a genuine high-period solution. To date, no such solutions have been found. Nevertheless, it is to be expected that they will occur in the present problem, associated with regions of chaos. However, they are likely to occur only in narrow bands of certain parameter values.

References

1. Virella JC, Prato CA, Godoy LA (2008) Linear and nonlinear 2D finite element analysis of sloshing modes and pressures in rectangular tanks subject to horizontal harmonic motions. J Sound Vib 312:442–460
2. Hermann M, Timokha A (2005) Modal modelling of the nonlinear resonant fluid sloshing in a rectangular tank I: a single-dominant model. Math Models Methods Appl Sci 15:1431–1458
3. Ibrahim RA, Pilipchuk VN, Ikeda T (2001) Recent advances in liquid sloshing dynamics. ASME Appl Mech Rev 54:133–199
4. Frandsen JB (2004) Sloshing motions in excited tanks. J Comput Phys 196:53–87
5. Chester W (1968) Resonant oscillations of water waves. I. Theory. Proc R Soc Lond A 306:5–22
6. Chester W, Bones JA (1968) Resonant oscillations of water waves. II. Experiment. Proc R Soc Lond A 306:23–39
7. Ockendon JR, Ockendon H (1973) Resonant surface waves. J Fluid Mech 59:397–413
8. Seydel R (1994) Practical bifurcation and stability analysis: from equilibrium to Chaos, second edition. Springer-Verlag Inc, New York
9. Hill DF (2003) Transient and steady-state amplitudes of forced waves in rectangular basins. Phys Fluids 15:1576–1587
10. Hill D, Frandsen J (2005) Transient evolution of weakly nonlinear sloshing waves: an analytical and numerical comparison. J Eng Math 53:187–198
11. Gardarsson SM, Yeh H (2007) Hysteresis in shallow water sloshing. J Eng Mech ASCE 133:1093–1100
12. Hermann M, Timokha A (2008) Modal modelling of the nonlinear resonant fluid sloshing in a rectangular tank II: secondary resonance. Math Models Methods Appl Sci 18:1845–1867
13. Amundsen DE, Cox EA, Mortell MP (2007) Asymptotic analysis of steady solutions of the KdVB equation with application to resonant sloshing. Z Angew Math Phys 58:1008–1034
14. Bredmose H, Brocchini M, Peregrine DH, Thais L (2003) Experimental investigation and numerical modelling of steep forced water waves. J Fluid Mech 490:217–249
15. Chen B-F, Nokes R (2005) Time-independent finite difference analysis of fully non-linear and viscous fluid sloshing in a rectangular tank. J Comput Phys 209:47–81
16. Wang CZ, Khoo BC (2005) Finite element analysis of two-dimensional nonlinear sloshing problems in random excitations. Ocean Eng 32:107–133
17. Celebi MS, Akyildiz H (2002) Nonlinear modeling of liquid sloshing in a moving rectangular tank. Ocean Eng 29:1527–1553
18. Armenio V, La Rocca M (1996) On the analysis of sloshing of water in rectangular containers: numerical study and experimental validation. Ocean Eng 23:705–739
19. Cariou A, Casella G (1999) Liquid sloshing in ship tanks: a comparative study of numerical simulation. Mar Struct 12:183–198
20. Liu D, Lin P (2008) A numerical study of three-dimensional liquid sloshing in tanks. J Comput Phys 227:3921–3939
21. Faltinsen OM, Rognebakke OF, Lukovsky IA, Timokha AN (2000) Multidimensional modal analysis of nonlinear sloshing in a rectangular tank with finite water depth. J Fluid Mech 407:201–234
22. Faltinsen OM, Timokha AN (2002) Asymptotic modal approximation of nonlinear resonant sloshing in a rectangular tank with small fluid depth. J Fluid Mech 470:319–357
23. Ikeda T (2007) Autoparametric resonances in elastic structures carrying two rectangular tanks partially filled with liquid. J Sound Vib 302:657–682
24. Forbes LK, Chen MJ, Trenham CE (2007) Computing unstable periodic waves at the interface of two inviscid fluids in uniform vertical flow. J Comput Phys 221:269–287
25. Forbes LK, Hocking GC (2007) Unsteady draining flows from a rectangular tank. Phys Fluids 19(082104), 14 pp
26. Atkinson KA (1978) An introduction to numerical analysis. Wiley, New York
27. Gradshteyn IS, Ryzhik IM (2000) Tables of integrals, series and products, 6th edn. Academic Press, San Diego
28. Abramowitz M, Stegun IA (eds) (1972) Handbook of mathematical functions. Dover Publications, Inc, New York
29. Kreyszig E (2006) Advanced engineering mathematics, 9th edn. Wiley, Singapore
30. Moore DW (1979) The spontaneous appearance of a singularity in the shape of an evolving vortex sheet. Proc R Soc Lond A 365:105–119
31. Cowley SJ, Baker GR, Tanveer S (1999) On the formation of Moore curvature singularities in vortex sheets. J Fluid Mech 378:233–267
32. Forbes LK (2009) The Rayleigh–Taylor instability for inviscid and viscous fluids. J Eng Math. doi:10.1007/s10665-009-9288-9